First Demonstration of Simultaneous Localization and Propulsion of a Magnetic Capsule in a Lumen using a Single Rotating Magnet

Katie M. Popek, Tucker Hermans, and Jake J. Abbott

***Abstract*— This paper presents a method for closed-loop propulsion of a screw-type magnetic capsule with embedded Hall-effect sensors using a single rotating actuator magnet. The method estimates the six-degree-of-freedom (6-DOF) pose of the capsule while it is synchronously rotating with the applied field. It is intended for application in active capsule endoscopy of the intestines. An extended Kalman filter, which uses a simplified 2-DOF process model restricting the capsule to forward or backward movement and rotation about its principle axis, is used to provide a full 6-DOF estimate of the capsule's pose as the capsule travels through a lumen. The capsule's movement in the applied field is constantly monitored to determine if the capsule is synchronously rotating with the applied field. Based on this information, the rotation speed of the external source is adjusted to prevent a loss in the desired magnetic coupling. We experimentally demonstrate, for the first time, simultaneous localization and closed-loop propulsion of a capsule through a lumen using a single rotating magnet. Prior work assumed the capsule had no net motion during the localization phase, requiring decoupled localization and propulsion. This closed-loop performance results in a three times speed up in completion time, compared to the previous decoupled approach.**

I. Introduction

Wireless capsule endoscopes, propelled by magnetic fields, promise a low-cost, minimally invasive method to view the entire gastrointestinal tract [1]. A small permanent magnet is embedded inside the capsule, and all power needed to propel the device is obtained from an externally applied magnetic field. Actuation methods typically use magnetic force for dragging or pulling [2]–[4] or screw-like propulsion of a capsule with a helical thread using magnetic torque [5]–[8]. Prior work from our lab developed a propulsion method for screw-type magnetic capsules using a single rotating magnetic dipole that can simultaneously employ magnetic force and torque [9]; this is the propulsion strategy that we utilize in this paper (Fig. 1).

One benefit of using magnetic fields for propulsion of capsule endoscopes is the opportunity for concurrent localization using the same magnetic field. There are several magnetic-localization methods previously published, see [10] for a review. We focus our discussion on those using *rotating* magnetic fields, as they are compatible with our chosen actuation method [9]. Additionally, their time-varying nature provides a constant influx of new information to the system, preventing the need for additional sensors (i.e., accelerometer). Prior localization methods typically assume the capsule has no net motion during localization [11], [12], which prevents continuous propulsion. Kim et al. [13] developed an algorithm to localize a capsule as it rotates with the applied field, but found in practice the capsule needed to be stationary to meet their desired performance [5]. Son et al. [14] describe a five-degree-of-freedom (5-DOF) localization algorithm using externally placed sensors to localize the capsule by measuring the field of the capsule's embedded permanent magnet, but to-date the workspace is limited.

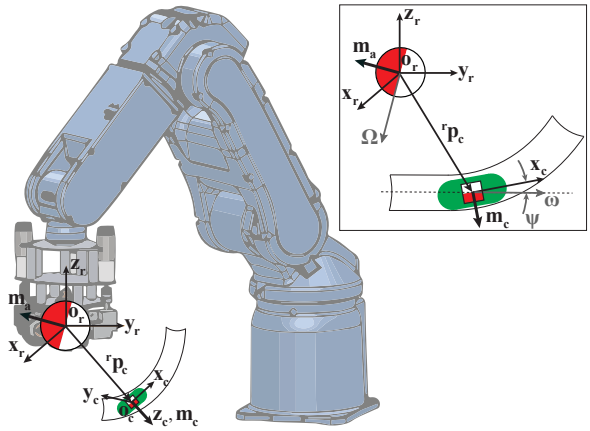

Fig. 1. Overall system setup with the external actuator magnet mounted on the end-effector of a robot. The capsule's coordinate frame origin $\mathbf{o}_c$ is placed at the center of its internal magnet, and the robot's tool frame origin $\mathbf{o}_r$ resides at the center of the actuator magnet. The inset depicts how the lumen will cause the principle axis of the capsule, $\mathbf{x}_c$, to lead the rotation axis of the applied field, $\boldsymbol{\omega}$, by some angle Ψ as the capsule is driven "forward". The turn is then sensed and incorporated by the extended Kalman filter to update the "forward" direction.

Prior work utilizing magnetic fields in true real-time closed-loop control of capsule endoscopes have dragged the capsule with magnetic forces [2]–[4]. Salerno et al. [3] developed a 2-DOF control system to measure forces during dragging tasks. Taddese et al. [2] experimentally demonstrated 4-DOF closed-loop control of a tethered magnetic capsule using magnetic field gradients. To the authors' knowledge, all prior closed-loop propulsion with rotating fields either utilized computer vision [9] for localization, which is not practical for clinical use, or required decoupled localization and propulsion [5]. Recently, we described a localization method to estimate the full 6-DOF pose of a magnetic capsule under the assumption of no net motion, and we applied the pose estimate for position and heading feedback in a proof-of-concept propulsion system [12]. The propulsion and localization were decoupled, similar to [5], such that propulsion was executed open-loop, and our capsule's movement was periodically paused for localization.

In this paper we present an extended Kalman filter (EKF)

K. M. Popek and T. Hermans are with the School of Computing, J. J. Abbott is with the Department of Mechanical Engineering, and all authors are with the Robotics Center, University of Utah, Salt Lake City, UT 84112, USA. email: katie.popek@utah.edu

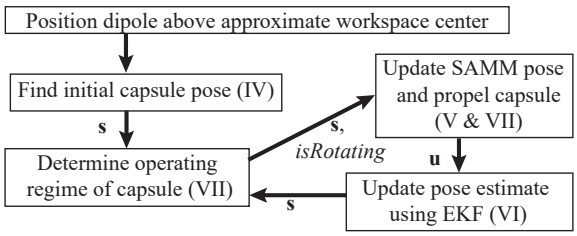

Fig. 2. Block diagram depicting our localization and propulsion system. **s** is the capsule's state, **u** is the system input, and *isRotating* is a Boolean representing whether the capsule is synchronously rotating with the field. Roman numerals correspond to the section in which each step is described.

to provide a continuous estimate of the capsule's 6-DOF pose as it rotates synchronously with an applied magnetic dipole field. The EKF uses a simplified 2-DOF process model that assumes the capsule movement is restricted to translation along and rotation about its principle axis. We restrict the remaining four degrees of freedom and let the lumen dictate changes in the capsule's heading. For example, as the capsule enters a turn, the geometry of the lumen will cause the capsule's axis $\mathbf{x}_c$ to deviate from the rotation axis of the applied field ($\boldsymbol{\omega}$) by an angle Ψ, as shown in the inset of Fig. 1. If Ψ is relatively small, the resulting restoring torque will be negligible and the capsule will continue to rotate because of compliance in the magnetic field. We have previously shown our propulsion method is robust to these types of misalignments [15]. The capsule's heading is updated based on the sensor measurements and the capsule is continually tracked throughout the curve.

This paper is also the culmination of many efforts from our group in magnetic capsule endoscopy. The capsule is initially localized using the method of [12]. It is propelled using the method of [9], with the permanent-magnet robotic end-effector described in [16]. Finally, the capsule's movement in the applied field is constantly monitored (i.e., Is the capsule synchronously rotating with the field, is the capsule able to rotate but the field is rotating too quickly for the capsule to remain rotating synchronously, or is the capsule stuck?), using the method described in [17]. A block diagram depicting the complete localization/propulsion system is shown in Fig. 2. The result is the first demonstration of simultaneous localization and propulsion of a screw-type magnetic capsule in a lumen using a single rotating magnet.

II. Nomenclature

Throughout this paper scalars are represented by italic lowercase font (e.g., s), vectors are denoted by lowercase bold font (e.g., ${}^{i}\mathbf{v}$) where the optional superscript i denotes a specific coordinate frame the vector is being expressed with respect to, and subscripts may also be used in the naming convention. The "hat" symbol (e.g., $\hat{\mathbf{v}}$) denotes a vector of unit length. Matrices are represented by uppercase bold font, and for rotation matrices ${}^{j}\mathbf{R}_i$ the subscript i and superscript j denote the starting and ending coordinate frames, respectively; this is also true for quaternions. $\mathbf{I}_n$ is an $n \times n$ identity matrix and $\mathbb{S}[\cdot]$ is the skew-symmetric matrix representation of the cross product operation (e.g., $\mathbb{S}[\mathbf{a}]\mathbf{b} = \mathbf{a} \times \mathbf{b}$).

III. Actuation and Sensing System

Our setup shown in Fig. 1 uses the Spherical-actuator-magnet Manipulator (SAMM) [16] mounted on the end-effector of a robotic arm for the external actuator magnet. The SAMM uses three mutually orthogonal omniwheels to generate singularity-free continuous rotation of its spherical magnet about arbitrary axes. The field of a spherical permanent magnet is nearly perfectly approximated by the point-dipole model. If a capsule is positioned in space at ${}^{r}\mathbf{p}_c$ the applied field ${}^{r}\mathbf{b}_c$ at the location of the capsule's magnet can be calculated with [18]:

$$ {}^{r}\mathbf{b}_c = \frac{\mu_0}{4\pi||{}^{r}\mathbf{p}_c||^5}\mathbf{B}_c\,{}^{r}\mathbf{m}_a \tag{1} $$

$$ \mathbf{B}_c = \left[3\,{}^{r}\mathbf{p}_c\,{}^{r}\mathbf{p}_c^T - \mathbf{I}_3||{}^{r}\mathbf{p}_c||^2\right] \tag{2} $$

where μ_0 is the permeability of free space and $\mathbf{m}_a$ is the magnetic moment of the actuator magnet.

There are six Hall-effect sensors rigidly placed inside the capsule, surrounding its internal magnet but minimally effected by its field, as described in [12], [17]. The position offset ${}^{c}\boldsymbol{\delta}_i$ of sensor i from the center of the capsule's magnet along with the orientation of the sensor's measuring axis ${}^{c}\boldsymbol{\alpha}_i$ are known and remain constant. The position vector to the i^{th} sensor from the robot's tool frame is calculated as

$$ {}^{r}\mathbf{p}_i = {}^{r}\mathbf{p}_c + {}^{r}\mathcal{Q}_c\,{}^{c}\boldsymbol{\delta}_i\,{}^{r}\mathcal{Q}_c^* \tag{3} $$

where ${}^{r}\mathcal{Q}_c$ is the quaternion representation of the rotation ${}^{r}\mathbf{R}_c$ (see Appendix A). The measurement of sensor i is the projection of the field onto the sensor's measuring axis:

$$ b_i = \frac{\mu_0}{4\pi||{}^{r}\mathbf{p}_i||^5}\,{}^{c}\boldsymbol{\alpha}_i^T\,{}^{r}\mathcal{Q}_c^*\left(\mathbf{B}_i\,{}^{r}\mathbf{m}_a\right){}^{r}\mathcal{Q}_c \tag{4} $$

IV. Initial Localization

The origin of the capsule's frame, $\mathbf{o}_c$, is located at the center of its internal magnet, and the origin of the robot's tool frame, $\mathbf{o}_r$, is placed at the center of the external dipole source, as shown in Fig. 1. We will solve for the capsule's 6-DOF pose, comprising position ${}^{r}\mathbf{p}_c$ and orientation ${}^{r}\mathbf{R}_c$, relative to the robot's tool frame. While it may be beneficial to transform the pose to a static world frame for clinical applications, in terms of controlling the capsule, the robot's tool frame is preferable because the magnetic equations are derived with respect to the actuator magnet.

To provide accurate tracking, we require an initial estimate of the capsule pose. From [12] we can determine the 6-DOF pose of a capsule with no net motion to within a few millimeters and a few degrees of the true capsule pose with no prior information. We modify the method for use with quaternions, since we previously employed the exponential formulation of a rotation matrix. Using the magnetic field measurements from the sensors embedded in the capsule, and rotating the external dipole about multiple orthogonal axes, it is possible to determine the capsule's 6-DOF pose relative to the external source (i.e., in the robot's tool frame).

The capsule's full 6-DOF pose is represented by a 7×1 state vector ${}^{r}\mathbf{s} = \left[{}^{r}\mathbf{p}_c^T\ {}^{r}\mathcal{Q}_c^T\right]^T$. The capsule's pose is

estimated by minimizing the cost function $||\mathbb{B}_m - \mathbb{B}_e||^2$ using the Levenberg-Marquardt algorithm. $\mathbb{B}_m$ is an array of the measured magnetic field readings corresponding to a single rotation of the dipole source about each of the $\mathbf{x}_r$, $\mathbf{y}_r$, and $\mathbf{z}_r$ axes, and $\mathbb{B}_e$ is an array of the magnetic field readings estimated by (4). As the initial position is unknown, five initial guesses, which are spread throughout the possible workspace, were used. The estimated pose resulting in the minimum norm of residual error between the estimated and measured sensor readings is chosen.

V. Propulsion Method

We summarize the method of [9]. If a dipole source $\mathbf{m}_a$ is rotated around some arbitrary axis $\hat{\mathbf{\Omega}}$ such that $\mathbf{m}_a^T \hat{\mathbf{\Omega}} = 0$ is always true, then at any point in space (e.g., the location of the capsule), the applied field rotates orthogonal to a local axis $\hat{\boldsymbol{\omega}}$. The rotation axis of the actuator magnet needed to provide a desired local rotation axis $\hat{\boldsymbol{\omega}}$ is calculated by:

$$ {}^r\hat{\mathbf{\Omega}} = \widehat{\mathbf{B}_c {}^r\hat{\boldsymbol{\omega}}} \tag{5} $$

where $\mathbf{B}_c$ is from (2). Assuming the capsule is constrained to a lumen, the desired $\hat{\boldsymbol{\omega}}$ is parallel to the capsule's principle axis $\mathbf{x}_c$ and locally aligned with the lumen. As $\mathbf{m}_a$ is rotated around $\hat{\mathbf{\Omega}}$, ${}^r\mathbf{b}_c$ rotates around $\hat{\boldsymbol{\omega}}$, updated as in (1), with the same period (but not necessarily the same instantaneous angular velocity). $\mathbf{B}_c$ requires an estimate of ${}^r\mathbf{p}_c$, and $\hat{\boldsymbol{\omega}}$ is an estimate of $\mathbf{x}_c$, these initially come from our estimate from Section IV, but are subsequently updated with our EKF.

VI. Extended Kalman Filter

We use a discrete-time implementation of the EKF [19], assuming constant inputs between samples, and assuming the following system model:

$$ \mathbf{s}_j = g(\mathbf{s}_{j-1}, \mathbf{u}_{j-1}, \mathbf{w}_{j-1}) \tag{6} $$

$$ \mathbf{y}_j = h(\mathbf{s}_j, \mathbf{u}_j, \mathbf{v}_j) \tag{7} $$

where $\mathbf{s}_j$ is the capsule's state at time step j, $\mathbf{u}_{j-1}$ is the input to the system at the previous time step, g models the system dynamics, $\mathbf{y}_j$ are the estimated observations, h is the measurement model, and $\mathbf{w}_j \sim (0, \mathbf{Q}_j)$ and $\mathbf{v}_j \sim (0, \mathbf{N}_j)$ are the zero-mean process and measurement noise parameters with known covariances of $\mathbf{Q}_j$ and $\mathbf{N}_j$, respectively. The EKF is broken into two steps: prediction and measurement update.

The *a priori* estimate predicts the next state $\mathbf{s}$ and its corresponding covariance $\mathbf{P}$ from the process model g and is denoted by the $-$ superscript.

$$ \mathbf{s}_j^- = g(\mathbf{s}_{j-1}^+, \mathbf{u}_{j-1}, \mathbf{w}_{j-1}) \tag{8} $$

$$ \mathbf{P}_j^- = \mathbf{G}_{j-1} \mathbf{P}_{j-1}^+ \mathbf{G}_{j-1}^T + \mathbf{Q}_{j-1} \tag{9} $$

where the state transition matrix $\mathbf{G}_{j-1}$ is defined as:

$$ \mathbf{G}_{j-1} = \left. \frac{\partial g}{\partial \mathbf{s}} \right|_{\mathbf{s}_{j-1}^+, \mathbf{u}_{j-1}} \tag{10} $$

The measurement update improves the *a priori* prediction by incorporating the observations to form the *a posteriori* state estimate, which is denoted with a $+$ superscript.

$$ \mathbf{K}_j = \mathbf{P}_j^- \mathbf{H}_j^T (\mathbf{H}_j \mathbf{P}_j^- \mathbf{H}_j^T + \mathbf{N}_j)^{-1} \tag{11} $$

$$ \mathbf{s}_j^+ = \mathbf{s}_j^- + \mathbf{K}_j (\mathbf{z}_j - h(\mathbf{s}_j^-, \mathbf{u}_j, 0)) \tag{12} $$

$$ \mathbf{P}_j^+ = (\mathbf{I}_7 - \mathbf{K}_j \mathbf{H}_j) \mathbf{P}_j^- \tag{13} $$

$$ \mathbf{H} = \left. \frac{\partial h}{\partial \mathbf{s}} \right|_{\mathbf{s}_j^-, \mathbf{u}_j} \tag{14} $$

where $\mathbf{z}_j$ is a vector of observations from time step j, $\mathbf{K}$ refers to the Kalman gain, and $\mathbf{H}$ is the Jacobian of the measurement model. The closed-form solutions for $\mathbf{G}$ and $\mathbf{H}$ are derived in Appendix B.

A. Process Model Implementation

The same state introduced in the initialization step is used in the EKF: ${}^r\mathbf{s} = [{}^r\mathbf{p}_c^T \ {}^r\mathcal{Q}_c^T]^T$. The system input consists of the actuator magnet's position and dipole orientation ${}^r\mathbf{u} = \left[{}^r\mathbf{o}_r^T \ {}^r\mathbf{m}_a{}^T\right]^T$. A simple 2-DOF process model is used to estimate how the capsule's state evolves over time, restricting translation to only forward or backward movement along $\mathbf{x}_c$, and rotation to only around $\mathbf{x}_c$. We rely on the constraining lumen to dictate the remaining degrees of freedom and assume the capsule's inertia and stiction are negligible. The capsule has a helical thread for propulsion, which translates magnetic force and torque into forward ($\mathbf{v}$) and angular ($\boldsymbol{\omega}$) velocity using the following symmetric matrix from [20]:

$$ \begin{bmatrix} \boldsymbol{\omega} \\ \mathbf{v} \end{bmatrix} = \begin{bmatrix} \mathbf{A} & \mathbf{E} \\ \mathbf{E}^T & \mathbf{L} \end{bmatrix} \begin{bmatrix} \boldsymbol{\tau} \\ \mathbf{f} \end{bmatrix} = \mathbf{\Gamma} \begin{bmatrix} \boldsymbol{\tau} \\ \mathbf{f} \end{bmatrix} \tag{15} $$

where $\mathbf{A}$, $\mathbf{E}$, and $\mathbf{L}$ are each 3×3 submatrices. The magnetic force and torque on the capsule from the applied magnetic field can be written as:

$$ {}^r\boldsymbol{\tau} = \frac{\mu_0}{4\pi ||{}^r\mathbf{p}_c||^5} {}^r\mathbf{m}_c \times (\mathbf{B}_c {}^r\mathbf{m}_a) = \frac{\mu_0}{4\pi ||{}^r\mathbf{p}_c||^5} \mathbb{S}[{}^r\mathbf{m}_c] \mathbf{B}_c {}^r\mathbf{m}_a \tag{16} $$

$$ {}^r\mathbf{f} = \frac{3\mu_0}{4\pi ||{}^r\mathbf{p}_c||^4} \left({}^r\mathbf{m}_a {}^r\mathbf{p}_c^T + {}^r\mathbf{p}_c {}^r\mathbf{m}_a^T + \left({}^r\mathbf{p}_c^T \mathbf{Z} {}^r\mathbf{m}_a \right) \mathbf{I}_3 \right) {}^r\mathbf{m}_c \tag{17} $$

where $\mathbf{Z} = \mathbf{I}_3 - 5 {}^r\hat{\mathbf{p}}_c {}^r\hat{\mathbf{p}}_c^T$.

The submatrices $\mathbf{A}$, $\mathbf{E}$, and $\mathbf{L}$ are chosen such that $\mathbf{\Gamma}$ only transfers the torque and force resulting in propulsion along ${}^c\mathbf{x}_c$ (the principle axis of the capsule).

$$ \mathbf{A} = \begin{bmatrix} a & 0 & 0 \\ 0 & 0 & 0 \\ 0 & 0 & 0 \end{bmatrix}, \mathbf{E} = \begin{bmatrix} e & 0 & 0 \\ 0 & 0 & 0 \\ 0 & 0 & 0 \end{bmatrix}, \mathbf{L} = \begin{bmatrix} l & 0 & 0 \\ 0 & 0 & 0 \\ 0 & 0 & 0 \end{bmatrix} \tag{18} $$

The scalar helical propulsion parameters are lumen dependent and were experimentally estimated prior to testing. Future work will involve developing an adaptive step to determine these parameters online. $\mathbf{\Gamma}$ was chosen to give the desired motion of the capsule in the capsule's coordinate frame, so $\boldsymbol{\omega}$ and $\mathbf{v}$ are calculated in that frame.

$$ \begin{bmatrix} {}^c\boldsymbol{\omega} \\ {}^c\mathbf{v} \end{bmatrix} = \mathbf{\Gamma} \begin{bmatrix} {}^r\mathcal{Q}_c^* {}^r\boldsymbol{\tau} {}^r\mathcal{Q}_c \\ {}^r\mathcal{Q}_c^* {}^r\mathbf{f} {}^r\mathcal{Q}_c \end{bmatrix} \tag{19} $$

Instead of updating the entire 7×1 state in a single function, the position and orientation are updated individually and combined:

$$g({}^r\mathbf{s}^+_{j-1}, {}^r\mathbf{u}_{j-1}) = \begin{bmatrix} g_{\mathbf{p}}({}^r\mathbf{s}^+_{j-1}, {}^r\mathbf{u}_{j-1})^T \\ g_{\mathcal{Q}}({}^r\mathbf{s}^+_{j-1}, {}^r\mathbf{u}_{j-1}) \end{bmatrix} \quad (20)$$

The position is updated using:

$$g_{\mathbf{p}}({}^r\mathbf{s}^+_{j-1}, {}^r\mathbf{u}_{j-1}) = {}^r\mathbf{p}_{c,j} = {}^r\mathbf{p}_{c,j-1} + \Delta t\, {}^r\mathcal{Q}_c\, {}^c\mathbf{v}\, {}^r\mathcal{Q}_c^* \quad (21)$$

The incremental change in orientation can be found by transforming the angular velocity into a unit quaternion.

$$\begin{gathered} {}^c\mathcal{Q}_{c,\Delta} = \cos\left(\frac{||{}^c\boldsymbol{\omega}||\Delta t}{2}\right) + \frac{{}^c\boldsymbol{\omega}}{||{}^c\boldsymbol{\omega}||}\sin\left(\frac{||{}^c\boldsymbol{\omega}||\Delta t}{2}\right) \\ g_{\mathcal{Q}}({}^r\mathbf{s}^+_{j-1}, {}^r\mathbf{u}_{j-1}) = {}^r\mathcal{Q}_{c,j} = {}^r\mathcal{Q}_{c,j-1}\, {}^c\mathcal{Q}_{c,\Delta} \end{gathered} \quad (22)$$

The process model noise is difficult to measure, so the covariance was tuned experimentally to provide desired tracking. All states are assumed independent, such that $\mathbf{Q}$ is non-zero only along its diagonal axis. Due to the slow nature of capsule endoscopy, we know the capsule's next position will be in close proximity to its previous position and place high certainty on the position's process model (the upper left 3×3 submatrix), which has units of m^2. The capsule's orientation is less certain because of the rotating fields and this is reflected in the chosen values (bottom right 4×4 submatrix), which are unitless:

$$\mathbf{Q} = \mathrm{diag}(0.001, 0.001, 0.001, 100, 100, 100, 100) \cdot 10^{-5}$$

B. Measurement Model Implementation

This method is a recursive variant of the original algorithm presented in [12] and similarly assumes there are n magnetic sensors rigidly embedded inside the capsule. The measurement model h estimates the sensor measurements by projecting the expected dipole field onto the sensor's measuring axis using (4). The n measurements are combined into a column vector:

$$h({}^r\mathbf{p}_c, {}^r\mathcal{Q}_c, {}^r\mathbf{m}_a, {}^c\mathbf{D}) = \begin{bmatrix} b_i({}^r\mathbf{p}_i, {}^r\mathcal{Q}_c, {}^r\mathbf{m}_a) \\ \vdots \\ b_n({}^r\mathbf{p}_n, {}^r\mathcal{Q}_c, {}^r\mathbf{m}_a) \end{bmatrix} \quad (23)$$

where ${}^c\mathbf{D}$ is a $3 \times n$ matrix where the i^{th} column corresponds to ${}^c\boldsymbol{\delta}_i$ and is used with ${}^r\mathbf{p}_c$ to calculate ${}^r\mathbf{p}_i$. Each row in h is calculated using (4).

The measurement noise covariance matrix $\mathbf{N}$ was estimated using sensor data from five locations spread throughout the workspace. Each sensor is assumed independent so the resulting values were placed along the diagonal of the 6×6 matrix, with the remaining values set to zero; the units are T^2.

$$\mathbf{N} = \mathrm{diag}(51.1, 49.4, 48.4, 57.2, 49.7, 59.1) \cdot 10^{-7}$$

VII. Detecting The Capsule's Operating Regime

At any given time, the capsule will be operating in one of three regimes. 1) The capsule is rotating synchronously with the applied field. 2) The capsule is in the "step-out" regime where the external field is rotated too quickly for the capsule to remain synchronously rotating. When this occurs the capsule rotates erratically back and forth trying to align with the field with little or no net motion. 3) The capsule is stuck (e.g., completely stationary). We only need to distinguish whether or not the capsule is synchronously rotating with the external field because the method of [12] can be used to estimate the pose of a capsule that is either stationary or in step-out. We have previously shown that knowledge of the "lead angle", ϕ, which is the angle between the applied field $\mathbf{b}_c$ and the capsule's dipole moment $\mathbf{m}_c$, is sufficient to distinguish this [17]. Briefly, if the lead angle remains relatively constant over a full rotation of the external field, the capsule must be synchronously rotating with the field, but if the capsule is stationary or in step-out, ϕ will periodically change signs. To prevent false positives that may occur when the capsule is rotating synchronously with a lead angle near zero, in addition to the sign change, the following condition must be met at least once in a given rotation to determine that the rotation is not synchronous: $|\phi| > \pi/2$ rad.

Given the capsule's estimated pose from either the initialization or the EKF, and whether the capsule is rotating with the applied field, the actuator dipole's pose is updated; pseudocode is given in Alg. I. If the capsule is not rotating with the field, the actuator's speed is slowed to 80 percent of the desired speed for two rotations to re-engage the capsule. If the capsule does not commence rotating with the field at this reduced speed, the actuator's speed is further decreased to 50 percent of the desired value. This was sufficient in our tested trajectories to always re-engage the capsule and begin forward motion. For more complex trajectories or in heterogeneous environments (e.g., intestines), additional steps may be required (e.g., using the uncertainty of the EKF's state estimate to re-localize if it is above a threshold).

VIII. Demonstration of Closed-loop Propulsion

In our experimental setup, the SAMM was mounted on the end-effector of a 6-DOF robotic arm and used as our external magnetic source. We used the prototype capsule introduced in [12] (Fig. 3(a)). It measures 42 mm in length and 13.5 mm in diameter not including the helix for propulsion. The capsule is embedded with six Allegro A1392 linear one-axis Hall-effect sensors arranged surrounding a $108\,\mathrm{mm}^3$ cubic NdFeB permanent magnet. The sensors are read at 100 Hz, but are wirelessly sent to the PC in batches at 20 Hz. The EKF is implemented as though each set of sensor data is received individually at the appropriate times.

Recently, we demonstrated a proof-of-concept propulsion system to confirm our localization estimates were sufficiently accurate using a decoupled magnetic propulsion and localization system [12]. Using this approach, the magnetic capsule successfully navigated through both a straight and curved lumen. For comparison, we demonstrate our simultaneous

Algorithm 1 Psuedocode to update the SAMM pose.

s is the estimated capsule state, *isRotating* is a Boolean representing the operating regime of the capsule, $||\mathbf{\Omega}||_{j-1}$ is the actuator's rotation speed at the prior time step, $\|\mathbf{\Omega}\|_{des}$ is the desired actuator rotation speed, t_r is the time required for the dipole source to complete two rotations, and $\mathbf{p}_{c,des}$ is the desired position offset between the capsule and the dipole source. It may be user specified (as it is here) or the result of an optimization routine.

```
1: ^r o_c ← s[1:3], ^w Q_c ← s[4:7]
2: ^r R_c ← QUATERNIONTOROTATIONMATRIX(^w Q_c)
3: ^r ω̂ ← ^r R_c(:, 1)
4: ^r o_r ← ^r o_c − ^r p_{c,des}
5: Ω̂ ← Eq. (5)
6: if isRotating then Ω_j = Ω̂_j ||Ω||_des, timer.STOP()
7: else
8:     if timer.NOTSTARTED() then timer.START()
9:     if timer.GETTIME() < t_r then Ω_j = 0.8 Ω̂_j ||Ω||_des
10:    else Ω_j = 0.5 Ω̂_j ||Ω||_des
```

localization and closed-loop propulsion system using the same trajectories, but continuously propel the capsule.

For the straight trajectory, a leading configuration matching that from [12] was chosen such that the capsule propulsion employs both an attractive magnetic force and magnetic torque. Figure 3(b) shows a composite image of the trajectory. With continuous actuation, the trajectory completion time was approximately 40 seconds with an average capsule speed of 6 mm/s, which is three times faster than what was reported in [12]. The 5-DOF error for the straight trajectory was found by comparing the capsule's estimated state from the EKF with that given by a stereo vision system. The average position error was 8.5 mm and 7.1°. The error on the roll angle is not reported because of difficulties accurately measuring the ground truth.

The semicircular trajectory from [12] was also reproduced to test the effectiveness of our 2-DOF process model. The SAMM was placed in an arbitrary position such that its relative placement with respect to the capsule remains constant as the capsule moves through the trajectory. This path had similar improvement over the decoupled propulsion/localization system from [12] with the trajectory taking approximately two minutes, less than a third of the original time (6.5 min), see Fig. 3(c); the average speed was 5.4 mm/s. Error is not reported because this trajectory was outside of the camera range.

For further demonstration, an additional test was completed in a Boston Scientific phantom of the small intestines (Fig. 3(d)). The current size of the capsule and SAMM's magnet prevent the capsule from moving through the stricture, but the capsule was successfully propelled through the curved ridged lumen with an average speed of 2.2 mm/s. At this speed, an examination of the entire small intestines would take approximately 45 minutes. In this experiment the SAMM is positioned at a desired offset with $\|\mathbf{p}_c\| = 100$ mm and $\hat{\mathbf{p}}_c$ dependent on the capsule's heading. As seen in the supplementary video, this choice resulted in significant movement of the SAMM because the capsule's heading changes as it traverses the phantom's ridges. In our current implementation, the capsule has trouble navigating near the tightest portion of the phantom's curve. Improving the robustness of the propulsion system based on the capsule's estimated state, optimizing the placement of the SAMM and its rotational speed, and improving the capsule's thread geometry are topics of future work to further increase the capsule's speed. The phantom and plastic tubing, although sufficient for a proof-of-concept, is not necessarily indicative of performance in real small intestines. Further testing is required in a soft, deformable lumen for a more accurate representation of the capsule's propulsion.

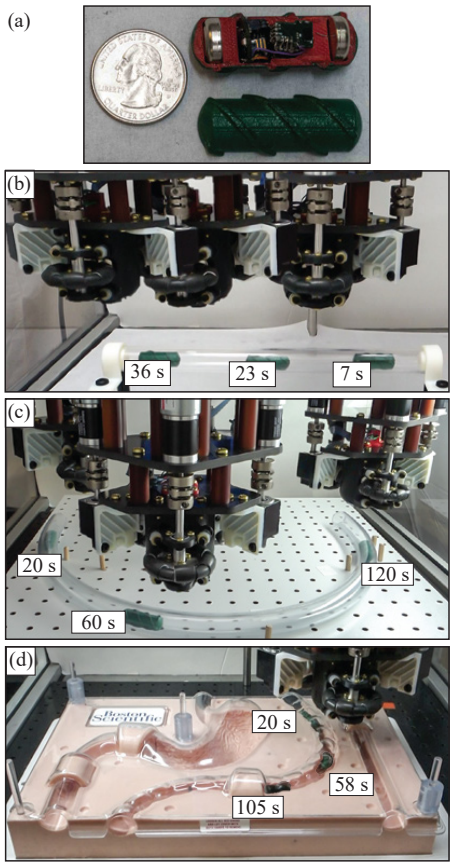

Fig. 3. Experimental demonstrations of simultaneous localization and closed-loop capsule propulsion. (a) Our prototype capsule embedded with a permanent magnet and six Hall-effect sensors was introduced in [12]. (b) To reproduce the trajectory originally demonstrated in [12], the SAMM was placed in a leading configuration with $\mathbf{p}_{c,des} = [0\ 58\ -100]$ mm and $\|\mathbf{\Omega}\|_{des} = 0.5$ Hz. (c). A reproduction of the semicircular path described in [12], with the SAMM placed in an arbitrary configuration with $\mathbf{p}_{c,des}$ a function of the capsule's heading such that the SAMM maintains the desired relative position as the capsule moves through the curve. $||\mathbf{p}_{c,des}|| = 100$ mm and $\|\mathbf{\Omega}\|_{des} = 0.5$ Hz. (d) The capsule was propelled through a Boston Scientific phantom. Similar to (c), $\|\mathbf{p}_c\| = 100$ mm with $\hat{\mathbf{p}}_c$ dependent on the capsule's heading, $\|\mathbf{\Omega}\|_{des} = 0.16$ Hz. Please see supplementary video.

IX. Conclusion

This paper provides the culmination of efforts in our group to enable active wireless capsule endoscopy by combining

magnetic propulsion, localization, and proprioceptive sensing into a single closed-loop propulsion-localization system. Our simplified 2-DOF process model is sufficiently accurate to model the capsule's dynamics through curved trajectories. We experimentally demonstrate, for the first time, continuous closed-loop propulsion of a magnetic screw-type capsule in a lumen using a single rotating magnet for both propulsion and localization. This presents an important step toward the use of rotating magnetic fields for capsule endoscopy.

Appendix A: Quaternion Review

Quaternions are an alternative to rotation matrices for representing orientations and rotations of Euclidean vectors [21]. Consider a rotation matrix $\mathbf{R}$, which can be represented in the angle-axis representation $(\theta, \hat{\mathbf{k}})$. A quaternion $\mathcal{Q}$ is a 4×1 vector that is constructed from the angle-axis representation:

$$\mathcal{Q} = \begin{bmatrix} q_0 \\ \mathbf{q} \end{bmatrix},\ q_0 = \cos\left(\frac{\theta}{2}\right),\ \mathbf{q} = \hat{\mathbf{k}}\sin\left(\frac{\theta}{2}\right) \tag{24}$$

where q_0 and $\mathbf{q}$ are the scalar and vector parts of the quaternion. A quaternion's conjugate is defined as

$$\mathcal{Q}^* = \begin{bmatrix} q_0 \\ -\mathbf{q} \end{bmatrix} \tag{25}$$

Quaternion multiplication is not commutative and is defined as:

$$\mathcal{Q}\cdot\mathcal{K} = \begin{bmatrix} q_0 & -\mathbf{q}^T \\ \mathbf{q} & q_0\mathbf{I}_3 - \mathbb{S}[\mathbf{q}] \end{bmatrix}\begin{bmatrix} k_0 \\ \mathbf{k} \end{bmatrix} \tag{26}$$

Quaternions can be used in a similar fashion to rotation matrices to rotate any arbitrary vector $\mathbf{r}$ into a different coordinate frame by conjugating $\mathbf{r}$ by $\mathcal{Q}$:

$${}^j\mathbf{r} = {}^j\mathcal{Q}_i\,{}^i\mathbf{r}\,{}^j\mathcal{Q}_i^* = \left(q_0^2 - \mathbf{q}\cdot\mathbf{q}\right){}^i\mathbf{r} + 2q_0\mathbf{q}\times{}^i\mathbf{r} + 2\mathbf{q}\left(\mathbf{q}\cdot{}^i\mathbf{r}\right) \tag{27}$$

The inverse rotation is performed in a similar way:

$${}^i\mathbf{r} = {}^j\mathcal{Q}_i^*\,{}^j\mathbf{r}\,{}^j\mathcal{Q}_i = \left(q_0^2 - \mathbf{q}\cdot\mathbf{q}\right){}^j\mathbf{r} + 2q_0\,{}^i\mathbf{r}\times\mathbf{q} + 2\mathbf{q}\left(\mathbf{q}\cdot{}^i\mathbf{r}\right) \tag{28}$$

Appendix B: Closed-form Jacobians

For compactness going forward, vectors are only given a frame label if they are **not** in the robot frame, $\mathbf{p} = \mathbf{p}_c$, and $\mathcal{Q} = {}^r\mathcal{Q}_c$. An explicit representation of the Jacobian matrix for the process model function, $\mathbf{G}(\mathbf{s},\mathbf{u})$ was derived and is given by:

$$\mathbf{G} = \begin{bmatrix} \frac{dg_\mathbf{p}}{d\mathbf{p}} & \frac{dg_\mathbf{p}}{d\mathcal{Q}} \\ \frac{dg_\mathcal{Q}}{d\mathbf{p}} & \frac{dg_\mathcal{Q}}{d\mathcal{Q}} \end{bmatrix} \tag{29}$$

where the four submatrices are defined below.

$$\frac{dg_\mathbf{p}}{d\mathbf{p}} = \frac{\partial g_\mathbf{p}}{\partial\mathbf{v}}\left(\frac{\partial\mathbf{v}}{\partial\mathbf{f}}\frac{\partial\mathbf{f}}{\partial\mathbf{p}} + \frac{\partial\mathbf{v}}{\partial\boldsymbol{\tau}}\frac{\partial\boldsymbol{\tau}}{\partial\mathbf{p}}\right) + \frac{\partial g_\mathbf{p}}{\partial\mathbf{p}} \tag{30}$$

$$\frac{dg_\mathbf{p}}{d\mathcal{Q}} = \frac{\partial g_\mathbf{p}}{\partial\mathbf{v}}\left(\frac{\partial\mathbf{v}}{\partial\mathbf{f}}\frac{\partial\mathbf{f}}{\partial\mathcal{Q}} + \frac{\partial\mathbf{v}}{\partial\boldsymbol{\tau}}\frac{\partial\boldsymbol{\tau}}{\partial\mathcal{Q}} + \frac{\partial\mathbf{v}}{\partial\mathcal{Q}}\right) + \frac{\partial g_\mathbf{p}}{\partial\mathcal{Q}} \tag{31}$$

$$\frac{dg_\mathcal{Q}}{d\mathbf{p}} = \frac{\partial g_\mathcal{Q}}{\partial\boldsymbol{\omega}}\left(\frac{\partial\boldsymbol{\omega}}{\partial\mathbf{f}}\frac{\partial\mathbf{f}}{\partial\mathbf{p}} + \frac{\partial\boldsymbol{\omega}}{\partial\boldsymbol{\tau}}\frac{\partial\boldsymbol{\tau}}{\partial\mathbf{p}}\right) \tag{32}$$

$$\frac{dg_\mathcal{Q}}{d\mathcal{Q}} = \frac{\partial g_\mathcal{Q}}{\partial\boldsymbol{\omega}}\left(\frac{\partial\boldsymbol{\omega}}{\partial\mathbf{f}}\frac{\partial\mathbf{f}}{\partial\mathcal{Q}} + \frac{\partial\boldsymbol{\omega}}{\partial\boldsymbol{\tau}}\frac{\partial\boldsymbol{\tau}}{\partial\mathcal{Q}} + \frac{\partial\boldsymbol{\omega}}{\partial\mathcal{Q}}\right) + \frac{\partial g_\mathcal{Q}}{\partial\mathcal{Q}} \tag{33}$$

The partial derivatives of (27) and (28) with respect to both $\mathcal{Q}$ and some arbitrary vector $\mathbf{r}$ are frequently used, so these are derived first.

$$\begin{aligned}
\Pi(\mathbf{r},\mathcal{Q}) &= \frac{\partial\mathcal{Q}\mathbf{r}\mathcal{Q}^*}{\partial\mathcal{Q}} = \begin{bmatrix}\frac{\partial\mathcal{Q}\mathbf{r}\mathcal{Q}^*}{\partial q_0} & \frac{\partial\mathcal{Q}\mathbf{r}\mathcal{Q}^*}{\partial\mathbf{q}}\end{bmatrix} \\
\frac{\partial\mathcal{Q}\mathbf{r}\mathcal{Q}^*}{\partial q_0} &= 2q_0\mathbf{r} + 2\mathbf{q}\times\mathbf{r} \\
\frac{\partial\mathcal{Q}\mathbf{r}\mathcal{Q}^*}{\partial\mathbf{q}} &= 2\left(q_0\mathbb{S}[\mathbf{r}]^T + \mathbf{q}\mathbf{r}^T + (\mathbf{q}\cdot\mathbf{r})\,\mathbf{I} - \mathbf{r}\mathbf{q}^T\right)
\end{aligned} \tag{34}$$

$$\begin{aligned}
\Pi^*(\mathbf{r},\mathcal{Q}) &= \frac{\partial\mathcal{Q}^*\mathbf{r}q\mathcal{Q}}{\partial q} = \begin{bmatrix}\frac{\partial\mathcal{Q}^*\mathbf{r}\mathcal{Q}}{\partial q_0} & \frac{\partial\mathcal{Q}^*\mathbf{r}\mathcal{Q}}{\partial\mathbf{q}}\end{bmatrix} \\
\frac{\partial\mathcal{Q}^*\mathbf{r}\mathcal{Q}}{\partial q_0} &= 2q_0\mathbf{r} + 2\mathbf{r}\times\mathbf{q} \\
\frac{\partial\mathcal{Q}^*\mathbf{r}\mathcal{Q}}{\partial\mathbf{q}} &= 2\left(q_0\mathbb{S}[\mathbf{r}] + \mathbf{q}\mathbf{r}^T + (\mathbf{q}\cdot\mathbf{r})\,\mathbf{I}_3 - \mathbf{r}\mathbf{q}^T\right) \\
\Upsilon^*(\mathcal{Q}) &= \frac{\partial\mathcal{Q}^*\mathbf{r}\mathcal{Q}}{\partial\mathbf{r}} = (q_0^2 - \mathbf{q}\cdot\mathbf{q})\mathbf{I}_3 + 2q_0\mathbb{S}[\mathbf{q}]^T + 2\mathbf{q}\mathbf{q}^T
\end{aligned} \tag{35}$$

Starting with (16), the partial derivative of $\boldsymbol{\tau}$ with respect to $\mathbf{p}$ and $\mathcal{Q}$ can be written as:

$$\frac{\partial\boldsymbol{\tau}}{\partial\mathcal{Q}} = \frac{\mu_0}{4\pi||\mathbf{p}||^5}\mathbb{S}[\mathbf{B}\mathbf{m}_a]^T\Pi({}^c\mathbf{m}_c,\mathcal{Q}) \tag{36}$$

$$\begin{aligned}
\frac{\partial\boldsymbol{\tau}}{\partial\mathbf{p}} &= c_\tau\left(\frac{3(\mathbf{p}^T\mathbf{m}_a\mathbf{I}_3 + \mathbf{p}\mathbf{m}_a^T + \mathbf{m}_a\mathbf{p}^T)}{\|\mathbf{p}\|^5} - \frac{15\mathbf{p}^T\mathbf{m}_a\mathbf{p}\mathbf{p}^T}{\|\mathbf{p}\|^7}\right) \\
c_\tau &= \frac{\mu_0\mathbb{S}[\mathcal{Q}^c\mathbf{m}_c\mathcal{Q}^*)]}{4\pi}
\end{aligned} \tag{37}$$

where $\mathbf{B}$ is from (1).

The partial derivative of the magnetic force (17) with respect to $\mathcal{Q}$:

$$\frac{\partial\mathbf{f}}{\partial\mathcal{Q}} = \frac{3\mu_0}{4\pi||\mathbf{p}||^4}\left(\mathbf{m}_a\hat{\mathbf{p}}^T + \mathbf{m}_a^T\hat{\mathbf{p}}\mathbf{I}_3 + \hat{\mathbf{p}}\mathbf{m}_a^T\mathbf{Z}^T\right)\Pi({}^c\mathbf{m}_c,\mathcal{Q}) \tag{38}$$

The derivative of force with respect to $\mathbf{p}$ is calculated as:

$$\begin{aligned}
\frac{\partial\mathbf{f}}{\partial\mathbf{p}} = \frac{3\mu_0\|\mathbf{m}_a\|\|\mathbf{m}_c\|}{4\pi\|\mathbf{p}\|^5}\Big(&\mathbf{X} - 5\hat{\mathbf{p}}\hat{\mathbf{p}}^T\mathbf{X} - 5\mathbf{X}\hat{\mathbf{p}}\hat{\mathbf{p}}^T - \\
&5\left(\hat{\mathbf{m}}_c^T(3\hat{\mathbf{p}}\hat{\mathbf{p}}^T - \mathbf{I}_3)\hat{\mathbf{m}}_a\right)\hat{\mathbf{p}}\hat{\mathbf{p}}^T\Big) \\
\mathbf{X} = \hat{\mathbf{m}}_a\hat{\mathbf{m}}_c^T + \hat{\mathbf{m}}_c\hat{\mathbf{m}}_a^T &+ \left(\hat{\mathbf{m}}_c^T\mathbf{Z}\hat{\mathbf{m}}_a\right)\mathbf{I}_3
\end{aligned} \tag{39}$$

Using the current values of $\boldsymbol{\tau}$ and $\mathbf{f}$, the partial derivatives of the forward and angular velocities are found:

$$\begin{aligned}
\frac{\partial\boldsymbol{\omega}}{\partial\boldsymbol{\tau}} &= \mathbf{A}\Upsilon^*(\mathcal{Q}),\ \frac{\partial\boldsymbol{\omega}}{\partial\mathbf{f}} = \mathbf{E}\Upsilon^*(\mathcal{Q}) \\
\frac{\partial\mathbf{v}}{\partial\boldsymbol{\tau}} &= \mathbf{E}^T\Upsilon^*(\mathcal{Q}),\ \frac{\partial\mathbf{v}}{\partial\mathbf{f}} = \mathbf{L}\Upsilon^*(\mathcal{Q})
\end{aligned} \tag{40}$$

where $\mathbf{A}$, $\mathbf{E}$, and $\mathbf{L}$ are from (18). The remaining partial derivatives for the position update are derived from (21):

$$\frac{\partial g_\mathbf{p}}{\partial\mathbf{v}} = \Delta t\left((q_0^2 - \mathbf{q}\cdot\mathbf{q})\mathbf{I}_3 + 2q_0\mathbb{S}[\mathbf{q}] + 2\mathbf{q}\mathbf{q}^T\right) \tag{41}$$

$$\frac{g_\mathbf{p}}{\partial\mathbf{p}} = \mathbf{I}_3 \tag{42}$$

$$\frac{\partial\mathbf{v}}{\partial\mathcal{Q}} = \mathbf{L}\Pi^*(\mathbf{f},\mathcal{Q}) + \mathbf{E}^T\Pi^*(\boldsymbol{\tau},\mathcal{Q}) \tag{43}$$

$$\frac{\partial g_{\mathbf{p}}}{\partial \mathcal{Q}} = \Pi(\mathbf{v}, \mathcal{Q})\Delta t \tag{44}$$

The following partial derivatives are calculated from the orientation update (22). $\mathcal{Q}_\Delta = [q_{\Delta,0}\ \mathbf{q}_\Delta^T]^T$ refers to the incremental change in orientation that is created using the capsule's speed as its rotation vector, $\boldsymbol{\upsilon} = \Delta t\boldsymbol{\omega}$. From [21], the derivative of a quaternion with respect to its rotation vector $\boldsymbol{\upsilon}$ is:

$$\frac{\partial \mathcal{Q}}{\partial \boldsymbol{\upsilon}} = \frac{1}{2||\boldsymbol{\upsilon}||^3}\begin{bmatrix} -\boldsymbol{\upsilon}_1\|\boldsymbol{\upsilon}\|^2 s & -\boldsymbol{\upsilon}_2||\boldsymbol{\upsilon}||^2 s & -\boldsymbol{\upsilon}_3||\boldsymbol{\upsilon}||^2 s \\ \sigma + \boldsymbol{\upsilon}_1^2\epsilon & \boldsymbol{\upsilon}_1\boldsymbol{\upsilon}_2\epsilon & \boldsymbol{\upsilon}_1\boldsymbol{\upsilon}_3\epsilon \\ \boldsymbol{\upsilon}_1\boldsymbol{\upsilon}_2\epsilon & \sigma + \boldsymbol{\upsilon}_2^2\epsilon & \boldsymbol{\upsilon}_2\boldsymbol{\upsilon}_3\epsilon \\ \boldsymbol{\upsilon}_1\boldsymbol{\upsilon}_3\epsilon & \boldsymbol{\upsilon}_2\boldsymbol{\upsilon}_3\epsilon & \sigma + \boldsymbol{\upsilon}_3^2\epsilon \end{bmatrix}$$
$$\text{where } c = \cos(\|\boldsymbol{\upsilon}\|/2),\ s = \sin(\|\boldsymbol{\upsilon}\|/2)$$
$$\epsilon = c\|\boldsymbol{\upsilon}\| - 2s,\ \sigma = 2||\boldsymbol{\upsilon}||^2 s \tag{45}$$

where the subscript on $\boldsymbol{\upsilon}$ refers to the vector index.

$$\frac{dg_{\mathcal{Q}}}{d\boldsymbol{\omega}} = \begin{bmatrix} q_0 & -\mathbf{q}^T \\ \mathbf{q} & q_0\mathbf{I} + \mathbb{S}[\mathbf{q}] \end{bmatrix}\frac{\partial \mathcal{Q}_\Delta}{\partial \boldsymbol{\upsilon}} \tag{46}$$

$$\frac{dg_{\mathcal{Q}}}{d\mathcal{Q}} = \begin{bmatrix} q_{\Delta,0} & -\mathbf{q}_\Delta^T \\ \mathbf{q}_\Delta & q_{\Delta,0}\mathbf{I} + \mathbb{S}[\mathbf{q}_\Delta]^T \end{bmatrix} \tag{47}$$

$$\frac{\partial \boldsymbol{\omega}}{\partial \mathcal{Q}} = \mathbf{E}\Pi^*(\mathbf{f}, \mathcal{Q}) + \mathbf{A}\Pi^*(\boldsymbol{\tau}, \mathcal{Q}) \tag{48}$$

An explicit representation of the Jacobian matrix for the measurement model, $\mathbf{H}(\mathbf{s}, \mathbf{u})$, is given by:

$$\mathbf{H} = \begin{bmatrix} \frac{\partial h}{\partial \mathbf{p}} & \frac{\partial h}{\partial \mathcal{Q}} \end{bmatrix} \tag{49}$$

The measurement model h_i can be rewritten in terms of $\mathbf{p}$ and $\mathcal{Q}$:

$$h_i = {}^c\boldsymbol{\alpha}^T\beta\mathcal{Q}^*\Lambda\mathcal{Q}^* \tag{50}$$

$$\text{where } \beta = \frac{\mu_0}{4\pi\|{}^r\mathbf{p} + \boldsymbol{\kappa}\|^5} \tag{51}$$

$$\Lambda = \left(3({}^r\mathbf{p} + \boldsymbol{\kappa})({}^r\mathbf{p} + \boldsymbol{\kappa})^T - \mathbf{I}_3\|{}^r\mathbf{p} + \boldsymbol{\kappa}\|^2\right)\mathbf{m}_a \tag{52}$$

where $\boldsymbol{\kappa} = \mathcal{Q}\,{}^c\boldsymbol{\delta}_i\mathcal{Q}^*$. By setting $\zeta = {}^c\boldsymbol{\alpha}^T\mathcal{Q}^*\Lambda\mathcal{Q}$ the partial derivative of h_i with respect to $\mathbf{p}$ is calculated as:

$$\frac{dh}{d\mathbf{p}} = \zeta\frac{\partial \beta}{\partial \mathbf{p}} + \beta\frac{\partial \zeta}{\partial \mathbf{p}} \tag{53}$$

$$\frac{\partial \zeta}{\partial \mathbf{p}} = {}^c\boldsymbol{\alpha}^T\Upsilon^*(\mathcal{Q})\frac{\partial \Lambda}{\partial \mathbf{p}} \tag{54}$$

$$\frac{\partial \Lambda}{\partial \mathbf{p}} = 3\left(\mathbf{I}_3\mathbf{p}^T\mathbf{m}_a + \mathbf{p}\mathbf{m}_a^T + \boldsymbol{\kappa}\mathbf{m}_a^T + \boldsymbol{\kappa}^T\mathbf{m}_a\mathbf{I}_3\right) - 2(\mathbf{m}_a\mathbf{p}^T + \mathbf{m}_a\boldsymbol{\kappa}^T) \tag{55}$$

$$\frac{\partial \beta}{\partial \mathbf{p}} = \left(\frac{-5\mu_0}{4\pi}\right)\frac{\mathbf{p}^T + \boldsymbol{\kappa}^T}{\|\mathbf{p} + \boldsymbol{\kappa}\|^7} \tag{56}$$

Similarly, the partial of h with respect to $\mathcal{Q}$ is:

$$\frac{dh}{d\mathcal{Q}} = \zeta\frac{d\beta}{d\mathcal{Q}} + \beta\frac{d\zeta}{d\mathcal{Q}} \tag{57}$$

$$\frac{d\zeta}{d\mathcal{Q}} = {}^c\boldsymbol{\alpha}^T\Upsilon^*(\mathcal{Q})\frac{\partial \Lambda}{\partial \mathcal{Q}} + {}^c\boldsymbol{\alpha}^T\Pi^*(\Lambda, \mathcal{Q}) \tag{58}$$

$$\frac{\partial \Lambda}{\partial \mathcal{Q}} = 3\big(\left(\mathbf{p}^T\mathbf{m}_a\mathbf{I}_3 + \boldsymbol{\kappa}\mathbf{m}_a^T + \boldsymbol{\kappa}^T\mathbf{m}_a\mathbf{I}_3 + \mathbf{p}\mathbf{m}_a^T\right) - 2\left(\mathbf{m}_a\mathbf{p}^T + \mathbf{m}_a\boldsymbol{\kappa}^T\right)\big)\Pi(\boldsymbol{\delta}_i, \mathcal{Q}) \tag{59}$$

$$\frac{d\beta}{d\mathcal{Q}} = \frac{\partial \beta}{\partial \mathbf{p}}\Pi(\boldsymbol{\delta}_i, \mathcal{Q}) \tag{60}$$

REFERENCES

[1] G. Ciuti, R. Caliò, D. Camboni, L. Neri, F. Bianchi, A. Arezzo, A. Koulaouzidis, S. Schostek, D. Stoyanov, C. M. Oddo, B. Magnani, A. Menciassi, M. Morino, M. O. Schurr, and P. Dario. Frontiers of robotic endoscopic capsules: a review. *Journal of Micro-Bio Robotics*, 11(1):1–18, 2016.

[2] A. Z. Taddese, P. R. Slawinski, K. L. Obstein, and P Valdastri. Closed loop control of a tethered magnetic capsule endoscope. In *Proc. of Robotics: Science and Systems*, 2016.

[3] M. Salerno, R. Rizzo, E. Sinibaldi, and A. Menciassi. Force calculation for localized magnetic driven capsule endoscopes. In *IEEE Int. Conf. Robotics and Automation*, pages 5354–5359, 2013.

[4] G. Ciuti, P. Valdastri, A. Menciassi, and P. Dario. Robotic magnetic steering and locomotion of capsule endoscope for diagnostic and surgical endoluminal procedures. *Robotica*, 28:199–207, 2010.

[5] J. Kim, Y. Kwon, and Y. Hong. Automated alignment of rotating magnetic field for inducing a continuous spiral motion on a capsule endoscope with a twistable thread mechanism. *Int. J. of Prec. Eng. & Manu.*, 13(3):371–377, 2012.

[6] A. Uchiyama, H. Kawano, K. Arai, K. Ishiyama, and M. Sendoh. Medical device guidance system, 2010. US Patent 7,711,408.

[7] Y. Zhang, S. Jiang, X. Zhang, X. Ruan, and D. Guo. A variable-diameter capsule robot based on multiple wedge effects. *IEEE/ASME Trans on Mech*, 16(2):241–254, April 2011.

[8] H. Zhou, G. Alici, T. D. Than, and W. Li. Modeling and experimental characterization of propulsion of a spiral-type microrobot for medical use in gastrointestinal tract. *IEEE Trans. Bio Eng*, 60(6):1751–1759, 2013.

[9] A. W. Mahoney and J. J. Abbott. Generating rotating magnetic fields with a single permanent magnet for propulsion of untethered magnetic devices in a lumen. *IEEE Trans. Robotics*, 30(2):411–420, 2014.

[10] T. D. Than, G. Alici, H. Zhou, and W. Li. A review of localization systems for robotic endoscopic capsules. *IEEE Trans. Bio. Eng.*, 59(9):2387–2399, 2012.

[11] E. Paperno, I. Sasada, and E. Leonovich. A new method for magnetic position and orientation tracking. *IEEE Trans. Magn.*, 37(4):1938–1940, 2001.

[12] K. M. Popek, T. Schmid, and J. J. Abbott. Six-degree-of-freedom localization of an untethered magnetic capsule using a single rotating magnetic dipole. *IEEE Robotics and Auto. Letters*, 2(1):305–312, 2017.

[13] M. Kim, Y. Hong, and E. Lim. Position and orientation detection of capsule endoscopes in spiral motion. *Int. J of Prec. Eng. and Manu.*, 11(1):31–37, 2010.

[14] D. Son, S. Yim, and M. Sitti. A 5-D localization method for a magnetically manipulated untethered robot using a 2-D array of hall-effect sensors. *IEEE Trans. Mech*, 21(2):708–716, 2016.

[15] A. W. Mahoney and J. J. Abbott. Control of untethered magnetically actuated tools with localization uncertainty using a rotating permanent magnet. In *IEEE Int. Conf. Biomedical Robotics and Biomechatronics*, pages 1632–1637, 2012.

[16] S. E. Wright, A. W. Mahoney, K. M. Popek, and J. J. Abbott. A spherical-magnet end-effector for robotic magnetic manipulation. In *IEEE Int. Conf. Robotics and Automation*, pages 1190–1195, 2015.

[17] K. M. Miller, A. W. Mahoney, T. Schmid, and J. J. Abbott. Proprioceptive magnetic-field sensing for closed-loop control of magnetic capsule endoscopes. In *IEEE Int. Conf. Intel. Robots & Sys.*, pages 1994–1999, 2012.

[18] E. P. Furlani. *Permanent magnet and electromechanical devices: materials, analysis, and applications*. Academic Press, San Diego, California, 2001.

[19] D. Simon. *Optimal State Estimation: Kalman, H Infinity, and Nonlinear Approaches*. John Wiley & Sons, 2006.

[20] J. J. Abbott, K. E. Peyer, M. Cosentino Lagomarsino, L. Zhang, L. X. Dong, I. K. Kaliakatsos, and B. J. Nelson. How should microrobots swim? *Int. J. Robotics Research*, 28(11-12):1434–1447, 2009.

[21] J. Diebel. Representing attitude: Euler angles, unit quaternions, and rotation vectors. *Matrix*, 58(15-16):1–35, 2006.

[22] A. W. Mahoney and J. J. Abbott. Five-degree-of-freedom manipulation of an untethered magnetic device in fluid using a single permanent magnet with application in stomach capsule endoscopy. *Int J Robotics Research*, 35(1–3):129–147, 2016.